


## Using helicity to investigate scalar transport in wall turbulence

Q. Nguyen and D. V. Papavassiliou \**School of Chemical, Biological, and Materials Engineering, The University of Oklahoma Norman, Norman, Oklahoma 73019, USA*

(Received 7 May 2019; accepted 7 May 2020; published 23 June 2020)

Helicity, defined as the inner product of the velocity and the vorticity vector, is elusive to measure even for laminar flows. Theoretical results for turbulence have shown that flow structures of high helicity are associated with low dissipation of kinetic energy, making them candidates for coherent structures that can persist longer than others in the flow field. As scalar transport in turbulence is enhanced by three-dimensional coherent motions, study of helicity could reveal flow structures that contribute more than others to scalar transport. Direct numerical simulations of turbulent channel flow at  $Re_\tau = 300$  in conjunction with Lagrangian tracking of fluid particles and passive scalar markers for Schmidt numbers 0.7 and 200 are used here. Local helicity along the trajectories of these markers and the fluid particles is calculated. Different levels of helicity are found to relate to the probability that these markers will remain inside a coherent region. The Lagrangian helicity distribution is also presented, indicating a change of the alignment between velocity and vorticity vectors for scalar transport markers.

DOI: [10.1103/PhysRevFluids.5.062601](https://doi.org/10.1103/PhysRevFluids.5.062601)

### I. INTRODUCTION

Scalar transport in turbulent flows plays a crucial role in turbulent mixing, chemical reactions, pollution, etc. Dispersion of aerosols in the atmosphere, moisture mixing in air, or mixing in water are typical examples of passive scalar transport in turbulence [1–5]. In the case of passive heat or mass transfer from a surface, it is known that multiple eddies participate in carrying a passive scalar away or towards the wall and contribute to dispersion into the flow field [6,7]. For scalar transport close to the wall, previous studies have indicated that only part of the turbulent spectrum contributes to transport, depending on the Prandtl or Schmidt number [8–13]. Among the flow structures that contribute to heat or mass transfer, the contributions are not equal. For scalars with small diffusivity, a large part of the spectrum, and thus of the turbulent structures, is not involved in turbulent transport, as it is harder for eddies to sweep heat or mass away from the wall.

How can those structures that contribute to turbulent dispersion be identified, and how can their contribution be quantified? In the case of high Reynolds number turbulence and in isotropic turbulence, these concerns are not as critical as they are for turbulent dispersion in anisotropic wall turbulence, where viscous effects can be quite important. The interplay between molecular and turbulent transport makes the overall process a function of molecular diffusivity, the Reynolds number, and the distance from the wall. Even scalar separation can occur under the combined effects of advection and molecular diffusion [14].

Eulerian simulations have focused on the eigenvectors of the rate of strain tensor relative to the direction of the gradient of the fluctuating scalar [15,16]. Vedula *et al.* [15] found that the fluctuating scalar gradient is more likely to be aligned with the eigenvector corresponding

\*Corresponding author: [dvpapava@ou.edu](mailto:dvpapava@ou.edu)

to the most compressive principal strain rate. Velocity-scalar correlation coefficients, conditional averaging, and spectral analysis have also been used. Lagrangian computations have also been employed, both by marking flow structures where Lagrangian markers reside [6,7] and by examining the eigenvectors of the Lagrangian correlation coefficient tensor for forwards and backwards (in time) turbulent dispersion [17]. A quantity that has not been explored as much is the helicity of the scalar-transporting flow structures.

Helicity is the inner product between the velocity and vorticity vectors. It has been explored for the study of flow topology and its correlation with turbulence transport, coherent structures, and energy cascade [18–25]. Regions with high values of helicity have a low-kinetic-energy dissipation rate, so that the flow structures in these regions would tend to persist in time, making them candidates for identifying coherent structures [18]. Several numerical studies have examined this theory and reported helicity; however, the results are still contradictory [26–29]. In any case, the experimental measurement of helicity is difficult, to the point of being infeasible. Recently, elegant experiments have been performed to measure helicity for laminar flows, reigniting the discussion about helicity [30]. In that work, vortices were created and visualized by accelerating 3D-printed hydrofoils of certain geometries in water and using fluorescent rhodamine dye. It was likely the first time that helicity dynamics could be measured in a viscous fluid, providing experimental insights to augment prior computational results.

Measuring helicity could help filter out regions of low vorticity in the flow field, as well as those areas of high vorticity but low momentum due to a large angle between the velocity and vorticity vectors, usually found in boundary layers [31]. While studies of helicity in turbulence have been carried out mostly with Eulerian simulations, this communication is focused on whether helicity can be used to mark flow structures that are major contributors to turbulent dispersion of scalars and to calculate helicity along the trajectories of Lagrangian markers of passive scalars. The goal is to reveal more information about the relationship between local vorticity, vortex structures, and scalar dispersion, as well as about the flow structures that are most important at different stages of the scalar dispersion process. We examine the hypothesis that helicity can be a superior identifier for scalar transport when employing a Lagrangian approach and that the correlation between velocity and vorticity along flow structures that are most effective in transferring heat or mass can be revealed.

## II. NUMERICAL METHODS

The turbulent flow field between two parallel plates has been simulated by using direct numerical simulation (DNS). The pseudospectral algorithm used herein has been presented and validated previously [32,33] for regular Poiseuille and Poiseuille-Couette flow [34]. All variables were dimensionless using the viscous wall units (i.e., the friction velocity  $u^*$  and the kinematic viscosity of the fluid  $\nu$ ). The computational box had dimensions of  $8\pi d \times d \times \pi d$  in the streamwise,  $x$ , normal,  $y$ , and spanwise,  $z$ , directions, respectively, with periodicity conditions applied in the  $x$  and  $z$  directions. The friction Reynolds number was  $Re_\tau = 300$ , given a half channel height ( $d/2$ ) of 300 in viscous wall units. The fluid was an incompressible Newtonian fluid with constant density and viscosity, while no-slip and no-penetration boundary conditions were imposed at the channel walls.

Lagrangian scalar tracking (LST) of mass markers was performed in conjunction with DNS. These passive markers represented scalar particles with no effect on the flow. The tracking algorithm has been presented earlier [35] and was used to track individual trajectories of these mass markers in space and time in a Lagrangian framework. The combined DNS-LST method has been used previously to study heat and mass transfer in high Schmidt or Prandtl number fluids [7,14,36,37]. Additional information about the accuracy of this method and comparisons of the results with experimental findings can be found in previous studies [8,38,39].

In the DNS-LST approach, the velocity field reached a stationary, fully developed state before releasing the mass markers. The Lagrangian velocity,  $\vec{V}(\vec{x}_0, t)$ , of a marker released at location  $\vec{x}_0$  at time  $t = t_0 = 0$  was assumed to be the same as the velocity of the fluid particle on which it rode

so that the relation between the Lagrangian velocity and the Eulerian velocity  $\vec{U}$  is  $\vec{V}(\vec{x}_0, t) = \vec{U}[\vec{X}(\vec{x}_0, t), t]$ . The mass markers, however, were allowed to move off a fluid particle due to molecular diffusion simulated by adding a random walk on the marker motion after each simulation time step. The magnitude of this diffusive motion was estimated by a Gaussian distribution in each direction in space with a zero mean and a standard deviation  $\sigma$ , depending on the Schmidt number  $Sc$  ( $\sigma = \sqrt{2\Delta t/Sc}$ ), where  $\Delta t$  is the simulation time step ( $\Delta t = 0.1$ ). This approach, based on Einstein's theory for Brownian motion [40], has been used successfully for different applications in heat and mass transfer [41–43], flow in porous media [44–48], and multiphase flow [49–51].

In the Eulerian frame of reference, helicity is defined as the volume integral of the dot product of velocity and vorticity vectors,

$$\mathcal{H} = \int \vec{U} \cdot \vec{W} dV, \quad (1)$$

where the vorticity is the curl of the velocity vector,  $\vec{W} = \nabla \times \vec{U}$ . When there is a balance between right-handed rotational motions and left-handed rotational motions in the flow,  $\mathcal{H}$  is equal to zero. Values of helicity could be positive or negative, depending on whether the helical motions are right-handed or left-handed. The integral kernel in Eq. (1) is defined as helicity density  $H$  as

$$H = \vec{U} \cdot \vec{W}. \quad (2)$$

Information about the alignment between velocity and vorticity vectors can be obtained by normalizing  $H$  with the magnitude of the velocity and vorticity vectors, thus introducing the relative helicity density  $h$  as

$$h = H/(|\vec{U}| * |\vec{W}|) = \cos \theta, \quad (3)$$

where  $\theta$  is the angle between the velocity and vorticity vectors.

Calculations were performed to obtain the helicity density along the trajectories of mass markers. Having already assumed that the velocity of a marker was the same as the velocity of the fluid at the markers' location, one can further assume that the value of the vorticity at the location of each marker is equal to the vorticity at the marker's position in the Eulerian framework, so that  $\vec{\omega}(\vec{x}_0, t) = \vec{W}[\vec{X}(\vec{x}_0, t), t]$ . The helicity density and relative helicity density at each marker location were defined as

$$H^p = \vec{V}(\vec{x}_0, t) \cdot \vec{\omega}(\vec{x}_0, t), \quad (4)$$

$$h^p = H^p/(|\vec{V}(\vec{x}_0, t)| * |\vec{\omega}(\vec{x}_0, t)|). \quad (5)$$

Two values of  $Sc$  were examined ( $Sc = 0.7, 200$ ) representing substances with three orders of magnitude different molecular diffusivities. In addition, fluid particles (molecular diffusion was taken to be zero) were included in the calculations to study the development of flow structures. Mass markers of each  $Sc$  were released at different locations,  $y_0 = 5, 15,$  and  $75$  wall units away from the bottom channel wall. This configuration would allow exploration of the effects of flow structures on scalar dispersion at different distances from the boundary. Possible bias because of peculiarities of the instantaneous velocity field were removed by releasing 100 000 markers from 20 lines spanning the  $x$ - $z$  plane at every  $y_0$  value. These lines were placed parallel to the spanwise direction and uniformly spaced along the  $x$  direction (at distances of  $8\pi d/20$ ). The markers were distributed uniformly in the  $z$  direction and were released in the flow field instantaneously and at the same time. As the flow field was homogeneous in the  $x$  and  $z$  directions, the exact location of each marker at the time of release was not statistically significant. The  $x$  location reported for each marker was calculated by subtracting the initial position  $x_0$  of the marker so that  $(x-x_0)$  was used as the marker location. Fluid particles were released in the same configuration as that of mass markers.

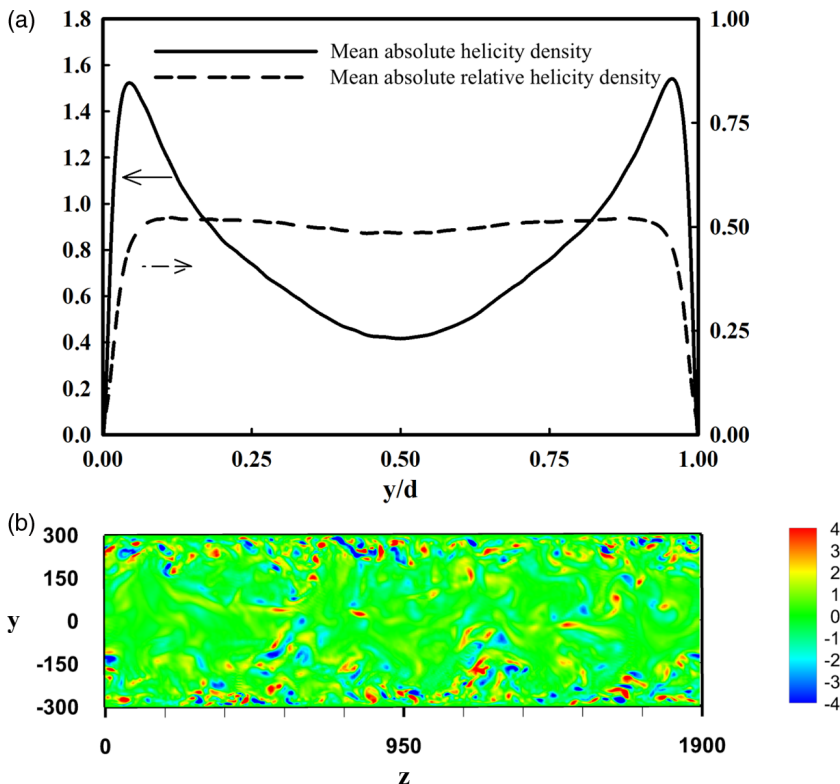


FIG. 1. (a) Mean absolute helicity density  $\overline{|H|}$  and mean absolute relative helicity density  $\overline{|h|}$  in the channel. (b) Contour plot of helicity density  $H$  on a  $y$ - $z$  plane (the mean flow direction is perpendicular to the  $y$ - $z$  plane).

### III. RESULTS

#### A. Helicity profile in channel flow

As previously mentioned, helicity  $\mathcal{H}$  is equal to zero. This is the result of the balanced distribution of left-handed and right-handed helical motions in the flow. Positive or negative helicity can have similar effects on scalar transport. Because of this, absolute values of helicity density,  $|H|$ , were used to detect helical motions and explore effects of flow structures on scalar dispersion.

Figure 1(a) is a plot of the mean of the absolute value of helicity density,  $\overline{|H|}$ , and the mean absolute values of relative helicity density,  $\overline{|h|}$ , along the vertical dimension in the channel. The profile of  $\overline{|H|}$  has a symmetric shape across the center line ( $y/d = 0.5$ ), with helicity density equal to 0 at the top and bottom walls as a result of the no-slip boundary condition. At the centerline,  $\overline{|H|}$  reaches a local minimum of 0.415. Two maxima of  $\overline{|H|}$  are observed at a distance of 25.7 wall units away from the nearest wall. As a comparison, locations of maximum turbulent kinetic energy production in channel flow were at 10.9 wall units measuring from the neighboring wall [34]. The two peaks of  $\overline{|H|}$  in Fig. 1(a) indicate areas of strong helical motions. In the wall region,  $\overline{|h|}$  is close to 0, indicating that the average angle between velocity and vorticity is close to  $90^\circ$ . Since the velocity used in this study is the instantaneous velocity, its vector is mostly parallel to the streamwise direction. At the wall region, it was found that spanwise vorticity is approximately 1.6 times larger than streamwise vorticity [34], indicating that the vorticity vector aligns better with the  $z$  direction, creating a large angle with the velocity vector. Farther away from the wall, the value of  $\overline{|h|}$  tends to approach a plateau of 0.5, indicating an average angle between velocity and vorticity of around  $60^\circ$ . This happens as the streamwise vorticity increases with distance from the wall compared to

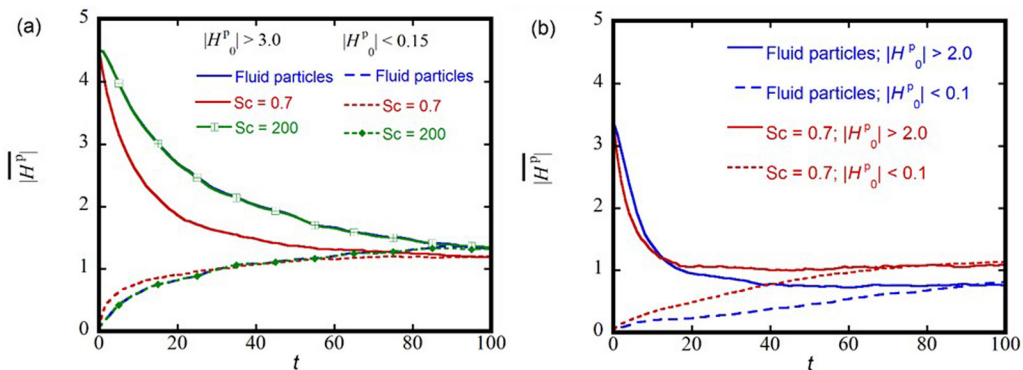


FIG. 2. Mean absolute helicity density of markers with different  $Sc$  and of fluid particles: (a) location of release at  $y_0^+ = 15$  and (b) location of release at  $y_0^+ = 5$ .

the spanwise vorticity, making the vorticity vector lean towards the streamwise direction and reduce the angle between velocity and vorticity. It should also be noted that  $|\overline{h}|$  reaches a plateau of 0.5 at  $y^+ \approx 40$  (the  $^+$  notation indicates inner scaling with viscous wall units), farther away from the wall than the location where the two peaks of  $|\overline{H}|$  were observed ( $y^+ \approx 25.7$ ). This indicates that not only the angle between velocity and vorticity, measured by relative helicity density, but also the magnitude of velocity and vorticity play an important role in the value of helicity. A contour plot of helicity density  $H$  is then presented in Fig. 1(b), showing a high density of helical motions in the wall region. The positive and negative values of  $H$  represent right-handed and left-handed helical motions in the flow.

### B. Scalar dispersion and helicity calculation in Lagrangian scheme

As already discussed, it has been proposed that regions with high helicity would correspond to a low-kinetic-energy dissipation rate. Flow structures in these regions would tend to persist in time, making them good candidates to identify coherent structures. One may expect that when found inside a coherent structure, markers of a passive scalar would travel with this structure until the structure dissipates. However, scalar markers can also jump out of a structure by molecular diffusion, before the structure dissipates. This makes the Lagrangian time scale different from the Eulerian time scale for coherent flow structures [52]. To study scalar transport in different flow structures, we categorize the markers based on initial helicity density and examine their dispersion as time advances. Markers with high helicity density are expected to stay within coherent flow structures and are compared to those having small helicity density. Specifically, two groups of markers that were released at  $y^+ = y_0^+ = 15$  were selected. Group 1 has  $H_0^p \geq 3$ , and group 2 has  $H_0^p \leq 0.15$  (where  $H_0^p = H^p$  at time  $t = t_0 = 0$ ) for markers with  $Sc = 0.7, 200$  and fluid particles. These two cutoff levels (3 and 0.15) were chosen so that approximately 10% of the markers released in the flow satisfy  $H_0^p \geq 3$  and another 10% would have  $H_0^p \leq 0.15$  at time  $t_0$ . For markers released at the edge of the viscous sublayer, at  $y_0^+ = 5$ , these two groups of particles were selected as those with  $H_0^p \geq 2$  and those with  $H_0^p \leq 0.10$ . The cutoff levels (2 and 0.10) were again chosen so that approximately 10% of the markers were captured in each group.

The average absolute helicity density of these two groups was measured as time increased and presented in Fig. 2, showing the change in helicity density along the markers' pathways. For release at  $y_0^+ = 15$  and markers with  $|H_0^p| \geq 3$ , their helicity density magnitude decreased with time and approached a plateau of approximately 1.3 at time  $t = 100$ , with a larger drop observed for markers with higher molecular diffusivity [see Fig. 2(a)]. The results of  $Sc = 200$  and fluid particles coincide, indicating that markers with very low molecular diffusivity behaved similarly to fluid particles in this flow region. For markers with  $|H_0^p| \leq 0.15$ , their helicity density increased with

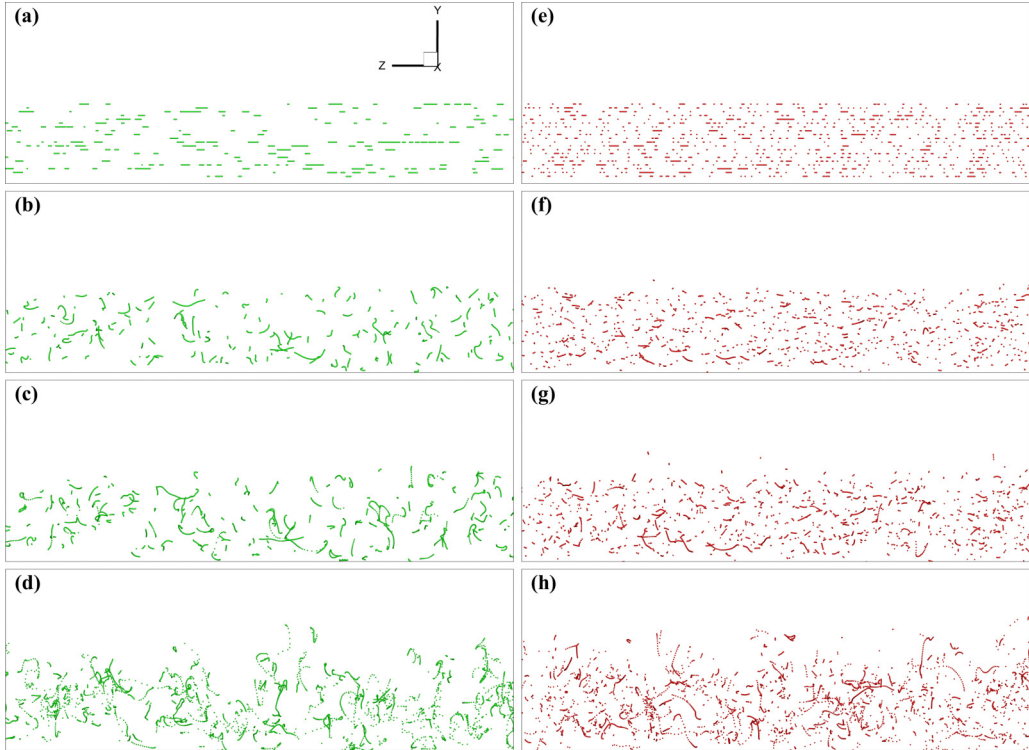


FIG. 3. Motion of fluid particles with  $|H_0^p| \geq 3$  at (a)  $t = 0$ , (b)  $t = 10$ , (c)  $t = 20$ , and (d)  $t = 50$ . Motion of fluid particles with  $|H_0^p| \leq 0.15$  at (e)  $t = 0$ , (f)  $t = 10$ , (g)  $t = 20$ , and (h)  $t = 50$ . (Animated videos are available online as Supplemental Material [53].)

time and reached a plateau of 1.3, merging with those markers with  $|H_0^p| \geq 3$ . Since the  $Sc = 200$  markers behave similarly to fluid particles, in Fig. 2(b) these markers are not shown. The results indicate that a plateau occurs but at different values for the fluid particles and the  $Sc = 0.7$  particles.

Motion of these markers during changes in their helicity density is visualized, giving a picture of the connection between helicity density and scalar dispersion. In Figs. 3(a)–3(d) the location of fluid particles with  $|H_0^p| \geq 3$  at different times is shown. The fluid particles follow flow structures, giving information about the motion of these structures. At time  $t = t_0 = 0$ , note that the particles are located close to each other. Since the initial placement of the scalar markers was on lines covering the  $x$ - $z$  plane, when a subset of them is identified to be released from regions of high local helicity, they are next to each other on a line segment, looking like beads on a string. The markers identified by high helicity values at the point of their release were found to move together, as seen in Figs. 3(a)–3(c). At longer times, these line segments start to break up, indicating that the particles move independently, corresponding to the dissipation of their helicity density indicated by the plateau in Fig. 2. This fact leads to the hypothesis that these markers were inside a flow structure that could carry them together. This is not coincidental, as a rather different picture was observed when visualizing the motion of markers released in locations of low helicity density [see Figs. 3(e)–3(h) for fluid particles released on locations with  $|H_0^p| \leq 0.15$ ]. First, fluid particles released in areas of low local values of helicity density are more dispersed. While some of them might participate in coherent motions, most of them appear to be moving alone. These observations are more clearly seen in the animations provided in the Supplemental Material [53].

One of the purposes here is to predict the most important flow structures contributing to scalar dispersion. By calculating relative helicity density  $h^p$ , the angle  $\theta^p$  between the markers' velocity

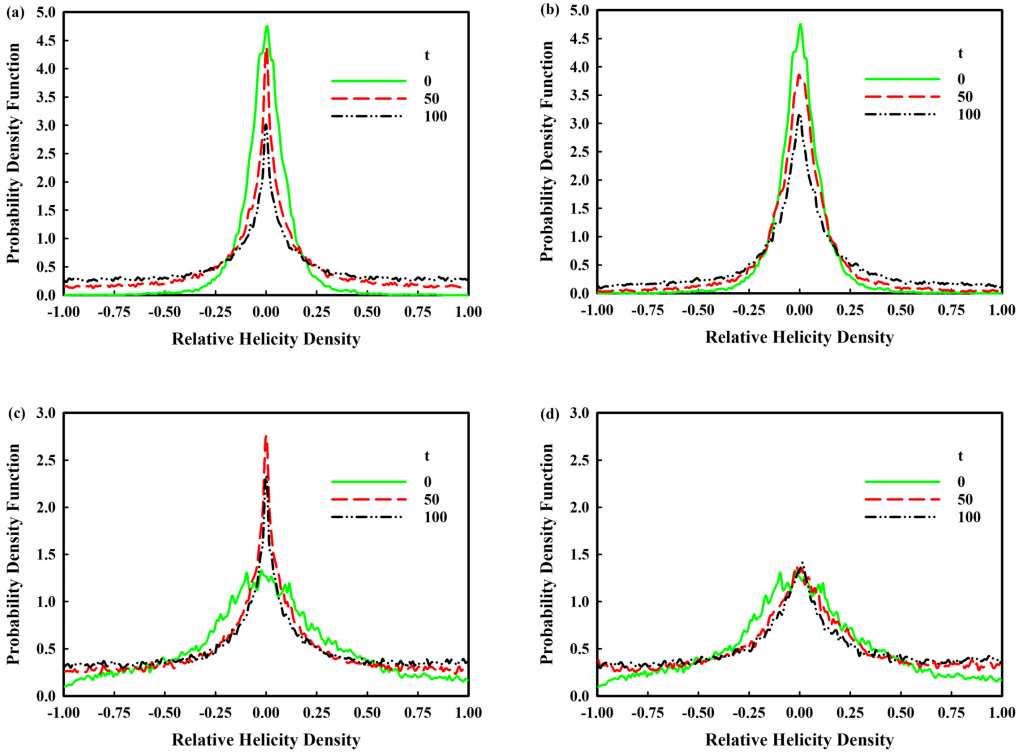


FIG. 4. Probability density function (PDF) of relative helicity density of markers: (a)  $Sc = 0.7$  released at  $y_0 = 5$ , (b) fluid particles released at  $y_0 = 5$ , (c)  $Sc = 0.7$  released at  $y_0 = 15$ , and (d) fluid particles released at  $y_0 = 15$ .

and vorticity vector could be estimated. This information can be used to identify the flow structures that are important at different stages of the scalar dispersion process. When  $h^p = 0$ , a marker's velocity is perpendicular to the local vorticity vector. We speculate that this happens when the marker is located at the edge of a vortex. It is calculated that  $h^p$  is close to 0 in the viscous wall layer. When  $h^p = \pm 1$ , the marker's velocity and vorticity vectors are parallel to each other (note that the sign simply indicates right-handed or left-handed rotational motions). The speculation for this case is that the markers are likely within the core of a vortex.

We present in Fig. 4 the probability density function (PDF) of relative helicity density for markers with  $Sc = 0.7$  and fluid particles traveling in the flow field, given different initial release locations ( $y_0^+ = 5$  and 15). In Figs. 4(a) and 4(b), it is seen that the PDFs for both  $Sc = 0.7$  and fluid particles, when released at  $y_0^+ = 5$ , display a peak at around 0 and at time  $t = t_0 = 0$ . This suggests that both  $Sc = 0.7$  and fluid particles were first in areas where the vorticity was approximately perpendicular to the markers' velocity. As time passes, the markers and fluid particles travel away from the viscous sublayer. There is an increase in the probability of them being carried by structures that have local vorticity in a direction parallel to the velocity. This could happen because of two reasons: the scalars jump to other flow structures aligned closely with the streamwise direction, or the initial structure develops to align closer with the streamwise direction, as in the case of developing hairpin vortices [54–56]. Since markers of  $Sc = 0.7$  have relatively large molecular jumps while fluid particles follow flow structures, the PDF of  $Sc = 0.7$  shows higher values at the two ends, indicating the jump of these markers to other flow structures or a move closer to the vortex core, leading to the increase of PDF values at  $\pm 1$ . This also explains why the shift in PDF values at  $\pm 1$  is not noticeable with fluid particles, as they have no diffusion and follow the same flow pattern.

The information in Figs. 4(c) and 4(d) shows a different picture. At time  $t = t_0 = 0$ , their PDFs are more flat between  $-0.5$  and  $0.5$ , indicating a more diverse range of vorticity in structures that carry them, compared to results seen in Figs. 4(a) and 4(b). As time increases, markers of  $Sc = 0.7$  show a PDF getting higher values at  $0$  and  $\pm 1$ . Therefore, the local vorticity vector and the local velocity vector tend to become either perpendicular or parallel to each other. We can speculate that when they are perpendicular, the markers would be at a location at the edge of a vortex, and when they are aligned, they would be at a vortex core. The behavior of fluid particles is different—the sharp peak at  $0$  is not seen to appear with time as is seen in Fig. 4(c).

#### IV. CONCLUSIONS

We presented here a method to measure helicity along the trajectories of Lagrangian markers of passive scalar transport. By analyzing values of helicity density and relative helicity density, more information about the interaction between particle dispersion and flow structures has been revealed. Not only markers located in regions of high vorticity were identified but also the alignment between markers' velocities and direction of vorticity were determined. The mean helicity density as a function of time indicates that there is a timescale associated with helicity that is about 100 viscous time units (see Fig. 2). Within this time, the average helicity density of fluid and scalar markers converges, even though the distribution of helicity is not the same (as seen in Fig. 4). By calculating the PDF of relative helicity density along trajectories of markers with  $Sc = 0.7$  and fluid particles released at the edge of the viscous sublayer, we found that the vorticity vector tends to be perpendicular to the velocity vector for most of the time. Therefore, the flow structures that are most important for the dispersion process rotate in a direction perpendicular to the direction of scalar transport. On the other hand, when the  $Sc = 0.7$  markers were released farther away from the wall ( $y_0^+ = 15$ ), a wider range of angles between velocity and vorticity was detected at first, followed by a shift towards either perpendicular or parallel alignment of the velocity and vorticity vectors of the fluid structures that carry these markers. The relative helicity density distribution of these markers changes with time (see Fig. 4), indicating that they move with flow structures that change with time. The fluid particles tend to be transported with structures that align their vorticity to the flow direction as time passes, while the low- $Sc$  markers are transported with structures where vorticity becomes perpendicular to the flow direction as time passes. The structures that contribute to the transport at low  $Sc$  are therefore different than those for fluid particles. Finally, it appears that analysis of turbulent transport based on helicity needs to be applied further in probing the coherent structures that are most effective in heat or mass transfer, and results will be presented in future work.

#### ACKNOWLEDGMENTS

Financial support of the National Science Foundation (Grant No. CBET-1803014) is gratefully acknowledged, as is the use of computing facilities at the University of Oklahoma Supercomputing Center for Education and Research and at XSEDE (under allocation CTS-090025).

- 
- [1] A. Khain, A. Pokrovsky, M. Pinsky, A. Seifert, and V. Phillips, Simulation of effects of atmospheric aerosols on deep turbulent convective clouds using a spectral microphysics mixed-phase cumulus cloud model, Part I: Model description and possible applications, *J. Atmos. Sci.* **61**, 2963 (2004).
  - [2] J. R. P. Hosker and S. E. Lindberg, Review: Atmospheric deposition and plant assimilation of gases and particles, *Atmos. Environ.* **16**, 889 (1982).



- [3] H. Suzuki, K. Nagata, Y. Sakai, and R. Ukai, High-Schmidt-number scalar transfer in regular and fractal grid turbulence, *Phys. Scr.* **2010**, 014069 (2010).
- [4] W. Y. Tam and H. L. Swinney, Mass transport in turbulent Couette-Taylor flow, *Phys. Rev. A* **36**, 1374 (1987).
- [5] R. R. Prasad and K. R. Sreenivasan, Quantitative three-dimensional imaging and the structure of passive scalar fields in fully turbulent flows, *J. Fluid Mech.* **216**, 1 (1990).
- [6] P. M. Le and D. V. Papavassiliou, A physical picture of the mechanism of turbulent heat transfer from the wall, *Int. J. Heat Mass Transfer* **52**, 4873 (2009).
- [7] A. K. Karna and D. V. Papavassiliou, Near-wall velocity structures that drive turbulent transport from a line source at the wall, *Phys. Fluids* **24**, 035102 (2012).
- [8] B. M. Mitrovic and D. V. Papavassiliou, Transport properties for turbulent dispersion from wall sources, *AIChE J.* **49**, 1095 (2003).
- [9] Y. Hasegawa and N. Kasagi, Low-pass filtering effects of viscous sublayer on high Schmidt number mass transfer close to a solid wall, *Int. J. Heat Fluid Flow* **30**, 525 (2009).
- [10] J. A. Campbell and T. J. Hanratty, Turbulent velocity fluctuations that control mass transfer to a solid boundary, *AIChE J.* **29**, 215 (1983).
- [11] J. A. Campbell and T. J. Hanratty, Mechanism of turbulent mass transfer at a solid boundary, *AIChE J.* **29**, 221 (1983).
- [12] Y. Na and T. J. Hanratty, Limiting behavior of turbulent scalar transport close to a wall, *Int. J. Heat Mass Transfer* **43**, 1749 (2000).
- [13] D. Lakehal, M. Fulgosi, G. Yadigaroglu, and S. Banerjee, Direct numerical simulation of turbulent heat transfer across a mobile, sheared gas-liquid interface, *J. Heat Transfer* **125**, 1129 (2003).
- [14] Q. Nguyen, C. Srinivasan, and D. V. Papavassiliou, Flow-induced separation in wall turbulence, *Phys. Rev. E* **91**, 033019 (2015).
- [15] P. Vedula, P. K. Yeung, and R. O. Fox, Dynamics of scalar dissipation in isotropic turbulence: A numerical and modelling study, *J. Fluid Mech.* **433**, 29 (2001).
- [16] W. T. Ashurst, A. R. Kerstein, R. M. Kerr, and C. H. Gibson, Alignment of vorticity and scalar gradient with strain rate in simulated Navier-Stokes turbulence, *Phys. Fluids* **30**, 2343 (1987).
- [17] C. Srinivasan and D. V. Papavassiliou, Direction of scalar transport in turbulent channel flow, *Phys. Fluids* **23**, 115105 (2011).
- [18] H. K. Moffatt, Helicity and singular structures in fluid dynamics, *Proc. Natl. Acad. Sci. USA* **111**, 3663 (2014).
- [19] H. K. Moffatt, Helicity in laminar and turbulent flow, *Annu. Rev. Fluid Mech.* **24**, 281 (1992).
- [20] H. K. Moffatt, Transport effects associated with turbulence with particular attention to the influence of helicity, *Rep. Prog. Phys.* **46**, 621 (1983).
- [21] N. Yokoi and A. Yoshizawa, Statistical analysis of the effects of helicity in inhomogeneous turbulence, *Phys. Fluids A* **5**, 464 (1993).
- [22] Q. Chen, S. Chen, and G. L. Eyink, The joint cascade of energy and helicity in three-dimensional turbulence, *Phys. Fluids* **15**, 361 (2003).
- [23] H. K. Moffatt, The degree of knottedness of tangled vortex lines, *J. Fluid Mech.* **35**, 117 (1969).
- [24] E. Levich and A. Tsinober, On the role of helical structures in three-dimensional turbulent flow, *Phys. Lett. A* **93**, 293 (1983).
- [25] A. Tsinober and E. Levich, On the helical nature of three-dimensional coherent structures in turbulent flows, *Phys. Lett. A* **99**, 321 (1983).
- [26] J. M. Wallace, J.-L. Balint, and L. Ong, An experimental study of helicity density in turbulent flows, *Phys. Fluids A* **4**, 2013 (1992).
- [27] M. M. Rogers and P. Moin, Helicity fluctuations in incompressible turbulent flows, *Phys. Fluids* **30**, 2662 (1987).
- [28] R. B. Pelz, L. Shtilman, and A. Tsinober, The helical nature of unforced turbulent flows, *Phys. Fluids* **29**, 3506 (1986).
- [29] R. B. Pelz, V. Yakhot, and S. A. Orszag, Velocity-Vorticity Patterns in Turbulent Flow, *Phys. Rev. Lett.* **54**, 2505 (1985).

- [30] M. W. Scheeler, W. M. v. Rees, H. Kedia, D. Kleckner, and W. T. M. Irvine, Complete measurement of helicity and its dynamics in vortex tubes, *Science* **357**, 487 (2017).
- [31] Y. Levy, D. Degani, and A. Seginer, Graphical visualization of vortical flows by means of helicity, *AIAA J.* **28**, 1347 (1990).
- [32] S. L. Lyons, T. J. Hanratty, and J. B. McLaughlin, Large-scale computer simulation of fully developed turbulent channel flow with heat transfer, *Int. J. Numer. Methods Fluids* **13**, 999 (1991).
- [33] A. Gunther, D. V. Papavassiliou, M. D. Warholic, and T. J. Hanratty, Turbulent flow in a channel at a low Reynolds number, *Exp. Fluids* **25**, 503 (1998).
- [34] Q. Nguyen and D. V. Papavassiliou, Turbulent plane Poiseuille-Couette flow as a model for fluid slip over superhydrophobic surfaces, *Phys. Rev. E* **88**, 063015 (2013).
- [35] K. Kontomaris and T. J. Hanratty, An algorithm for tracking fluid particles in a spectral simulation of turbulent channel flow, *J. Comput. Phys.* **103**, 231 (1992).
- [36] C. Srinivasan and D. V. Papavassiliou, Prediction of the turbulent Prandtl number in wall flows with Lagrangian simulations, *Ind. Eng. Chem. Res.* **50**, 8881 (2011).
- [37] D. V. Papavassiliou, Scalar dispersion from an instantaneous line source at the wall of a turbulent channel for medium and high Prandtl number fluids, *Int. J. Heat Fluid Flow* **23**, 161 (2002).
- [38] D. V. Papavassiliou and T. J. Hanratty, Transport of a passive scalar in a turbulent channel flow, *Int. J. Heat Mass Transfer* **40**, 1303 (1997).
- [39] D. V. Papavassiliou, Turbulent transport from continuous sources at the wall of a channel, *Int. J. Heat Mass Transfer* **45**, 3571 (2002).
- [40] A. Einstein, Über die von der molekular-kinetischen Theorie der Wärme geforderte Bewegung von in ruhenden Flüssigkeiten suspendierten Teilchen, *Ann. Phys.* **322**, 549 (1905).
- [41] K. Kontomaris and T. J. Hanratty, Effect of molecular diffusivity on point source diffusion in the center of a numerically simulated turbulent channel flow, *Int. J. Heat Mass Transfer* **37**, 1817 (1994).
- [42] Y. Mito and T. J. Hanratty, Lagrangian stochastic simulation of turbulent dispersion of heat markers in a channel flow, *Int. J. Heat Mass Transfer* **46**, 1063 (2003).
- [43] Y. Hasegawa and N. Kasagi, The effect of Schmidt number on air-water interface mass transfer, in *Proceedings of the 4th International Conference on Multiphase Flow, New Orleans, LA* (Elsevier, New York, 2001).
- [44] M. M. Tomadakis and D. Rupani, Diffusion controlled reaction rate, survival probability, and molecular trajectory characteristics in the bulk, transition and Knudsen regime, *Chem. Eng. J.* **128**, 1 (2007).
- [45] R. S. Voronov, S. B. VanGordon, V. I. Sikavitsas, and D. V. Papavassiliou, Efficient Lagrangian scalar tracking method for reactive local mass transport simulation through porous media, *Int. J. Numer. Methods Fluids* **67**, 501 (2011).
- [46] N. H. Pham and D. V. Papavassiliou, Effect of spatial distribution of porous matrix surface charge heterogeneity on nanoparticle attachment in a packed bed, *Phys. Fluids* **29**, 082007 (2017).
- [47] N. H. Pham and D. V. Papavassiliou, Hydrodynamic effects on the aggregation of nanoparticles in porous media, *Int. J. Heat Mass Transfer* **121**, 477 (2018).
- [48] R. S. Voronov, S. B. VanGordon, V. I. Sikavitsas, and D. V. Papavassiliou, Computational modeling of flow-induced shear stresses within 3D salt-leached porous scaffolds imaged via micro-CT, *J. Biomech.* **43**, 1279 (2010).
- [49] S. S. Ponoth and J. B. McLaughlin, Numerical simulation of mass transfer for bubbles in water, *Chem. Eng. Sci.* **55**, 1237 (2000).
- [50] R. Verberg, A. Alexeev, and A. C. Balazs, Modeling the release of nanoparticles from mobile microcapsules, *J. Chem. Phys.* **125**, 224712 (2006).
- [51] G. V. Kolmakov, R. Revanur, R. Tangirala, T. Emrick, T. P. Russell, A. J. Crosby, and A. C. Balazs, Using nanoparticle-filled microcapsules for site-specific healing of damaged substrates: Creating a “repair-and-go” system, *ACS Nano* **4**, 1115 (2010).
- [52] P. G. Saffman, On the effect of molecular diffusivity in turbulent diffusion, *J. Fluid Mech.* **8**, 273 (1960).
- [53] See Supplemental Material at <http://link.aps.org/supplemental/10.1103/PhysRevFluids.5.062601> for animated videos of the fluid particle dispersion at high- and low-helicity regions.

- [54] M. S. Acarlar and C. R. Smith, A study of hairpin vortices in a laminar boundary layer, Part 1. Hairpin vortices generated by a hemisphere protuberance, [J. Fluid Mech. 175, 1 \(1987\)](#).
- [55] T. Theodorsen, in *Proceedings of the Midwestern Conference of Fluid Mechanics*, Ohio State University, Columbus, OH (Engineering Experiment Station, Ohio State University, Columbus, OH, 1952), p. 18.
- [56] S. K. Robinson, Coherent motions in the turbulent boundary layer, [Annu. Rev. Fluid Mech. 23, 601 \(1991\)](#).